

K.P. Geigle, W. O'Loughlin, R. Hade¹, W. Meier, Visualization of soot inception in turbulent pressurized flames by simultaneous measurement of laser-induced fluorescence of polycyclic aromatic hydrocarbons and laser-induced incandescence, and correlation to OH distributions, Appl. Phys. B 119 (2015) 717-730.

¹ Université Larbi Ben M'Hidi Institut de Génie Mécanique, Oum El Bouaghi, Algeria

The original publication is available at www.springerlink.com

<http://dx.doi.org/10.1007/s00340-015-6075-3>

Visualization of soot inception in turbulent pressurized flames by simultaneous measurement of laser-induced fluorescence of polycyclic aromatic hydrocarbons and laser-induced incandescence, and correlation to OH distributions

Shortened version: Correlated PAH LIF and LII to visualize soot inception in turbulent pressurized flames

Klaus Peter Geigle¹, William O'Loughlin¹, Redjem Hade², Wolfgang Meier¹

¹Institute of Combustion Technology, German Aerospace Center
Pfaffenwaldring 38-40, 70569 Stuttgart, Germany

²Université Larbi Ben M'Hidi, Institut de Génie Mécanique
04000 Oum El Bouaghi, Algeria

Phone: +49-711-6862-398

Fax: +49-711-6862-578

Email: klauspeter.geigle@dlr.de

Abstract

Distributions of polycyclic aromatic hydrocarbons (PAH) and their correlation with soot formation were studied in ethylene-air swirl flames stabilized in a gas turbine model combustor at increased pressure. The combustor can be operated with secondary air injection to study the influence of soot oxidation. We employed PAH laser-induced fluorescence using UV excitation simultaneously with IR-excited laser-induced incandescence to identify soot. PAH signatures typically appear discontinuous unlike OH, yet similar to soot but exhibit more uniform intensity and larger size. The correlation of both diagnostics allowed identification of a wide range of soot formation progress, including isolated soot or PAH, as well as PAH transitioning into soot. The occurrence of soot, PAH and OH and their spatial variations are strongly dependent on the properties of the flow field. In the bottom part of the inner recirculation zone and for the reference case, a rich flame with additional oxidation air, soot levels are relatively high while PAH intensities in this region are minimal. This correlates well with high temperatures in this region published recently, which are unfavorable for soot formation as the precursors, PAH, decompose. Consequently, soot presence here is attributed to transport. In contrast to OH and soot distributions which change significantly upon addition of secondary air downstream of the primary combustion zone, PAH distributions for both cases look relatively similar. This is attributed to a downstream consumption of PAH by different processes. Without oxidation air, PAH completely transform into soot, while additional oxidation air leads to their oxidation.

1. Introduction

Soot emissions from technical combustion devices constitute a serious environmental and human health problem [1-3] whose solution requires coordinated efforts from scientists and engineers, including computational and experimental methods. Numerical simulation is expected to provide significant contributions to future combustor development. With respect to soot modelling of turbulent flames in real aero-engine combustors, different approaches have been used, particularly

Unsteady Reynolds Averaged Navier Stokes (URANS) models, for example demonstrated in Ref. [4] using transported chemistry, or Large Eddy Simulation (LES), for example with tabulated chemistry [5]. Highly challenging is the prediction of soot formation and oxidation in aero-engine combustors due to the huge complexity involving a sophisticated combustor geometry, high pressure and turbulence levels, radiation and a comprehensive combustion and soot chemistry that is even further complicated by the complex fuel composition. Beyond that, the boundary conditions are far from well-defined and thus partly have to be assumed [6]. Considering this difficult task, it appears sensible to choose a gradual approach from simple flames to systems with increasing complexity. Furthermore, the availability of reliable experimental validation data is essential for the assessment and improvement of the models. The data sets should include the important quantities, cover the range from simple to technical flames and various fuels and must be measured at well-defined boundary conditions.

Best accessible for comprehensive application of accurate diagnostics are simple laminar flames, which have been characterized in great detail. A number of sooting laminar premixed [7-13] or diffusion flames [14-18, 19-29] have been selected as target flames by the modelling community within the “International Sooting Flame Workshop” [30]. The influence of turbulence has been investigated in turbulent jet flames, such as described in Refs. [31-35]. Those flames were more challenging to study experimentally due to higher thermal loads, larger dimensions, longer measurement series for a good statistics and the requirement of good temporal and spatial resolution. However, not in all cases the data sets were suitable for model validation due to the lack of important quantities like flow field or temperature distributions.

One step further in complexity was achieved by measurements in swirled pressurized flames. Geigle et al. [36] determined quantitative soot distributions for several C_2H_4 flames. In a subsequent study OH distributions and temperature statistics, as well as correlations of OH and soot were analyzed for a subset of those flames [37]. That work was mainly focused on the impact of additional quench or oxidation air which was injected downstream of the primary combustion zone. This air mimicked the cooling or quench air in an aero-engine combustor. It was shown that the additional air was partly mixed into the inner recirculation zone and reached far upstream influencing soot formation close to the burner inlet as well as OH and temperature distributions in the inner recirculation zone. The detailed data set has been used for model validation [4,38,39] and can be made available to other researchers.

Soot formation is assumed to proceed via large precursor species, polycyclic aromatic hydrocarbons (PAH), in combination with acetylene [40]. Details about the transition from the molecular to the particle-like regime, or the gas-phase to the liquid/solid phase, respectively, are still a topic of discussion. A detailed overview of this issue, combined with an extensive discussion of existing minimally intrusive diagnostics focusing on the molecular size range close to this transition is provided by Desgroux et al. [41]. Unlike simple molecules as for example OH, detailed quantitative information on selected PAH species in flames is difficult to obtain by optical techniques. This is due to the huge number of different PAH molecules, their very different and typically low specific concentrations, and strongly varying spectroscopic behavior which depends on the local temperature and gas composition. In addition, their absorption and emission spectra are broad and strongly overlapping at typical flame conditions. Therefore, mostly PAH classes rather than individual species have been studied by laser-induced fluorescence by various research groups. Vander Wal [42] identified an isolated PAH layer, separated from soot by a dark zone, both in a droplet flame and an

inverted diffusion flame by comparing the optical emissions after IR (exciting soot alone) and UV excitation at 266 nm (exciting both soot and PAH). The author interpreted this area as transition region into soot. A similar experiment was performed by Schoemaecker et al. simultaneously using 532 and 1064 nm excitation [43]. Despite visualization of a larger size class of PAH upon visible excitation, a dark zone of low laser-induced emission between PAH and soot remained detectable. Different types of stationary and flickering diffusion flames were characterized by simultaneous application of soot and PAH visualization, eventually leading to a detailed comparison of the soot formation process in inverted and normal diffusion flames [44,45]. Recent examples of the application of PAH LIF to turbulent jet flames include the work by Lee et al. [32], Köhler et al. [35] and Zhang et al. [34]. The latter monitored PAH as JP-8 fuel component in OH LIF experiments, thus visualizing the correlation of OH and fuel. PAH as component in kerosene enables in principle the detection of fuel distributions in technical combustors by LIF, however, this is not the focus of this overview. Lee and co-workers, in contrast, performed a detailed analysis of combustion-generated PAH, OH and soot, and identified three different and distinct regions of soot formation and oxidation. The statistics of those three species were correlated (although not simultaneously measured), and showed that PAH were typically present close to the flame axis in the upstream half of the flame, enclosed by soot and radially further outside by OH. The region of PAH detection was identified as soot formation zone. Along the downstream half of the jet flame, OH and soot zones overlapped due to turbulent motion and mixing, leading to soot oxidation and significant decrease of PAH intensities. The distinct zones associated with soot formation/destruction regions were further studied by analyzing OH and soot sheet thickness statistics and further correlated with temperature statistics derived by coherent anti-Stokes Raman scattering (CARS). In this very comprehensive study the authors applied PAH excitation at about 283 nm and report relatively low PAH signal. A very recent in-cylinder application in an optically accessible diesel engine employed different excitation wavelengths to analyze the progress of molecular growth of PAH species into soot in a transient process on a statistical basis [46]. The crank angle dependence allowed studying the temporal evolution in this case. In contrast to this, stationary processes exhibit all these soot formation stages at the same time and different location in the combustor, or at the same location but different instances in time. It is noted that PAH species can be measured with good species selection by mass spectrometry or sampling followed by jet-cooled laser-induced fluorescence [41,47,48], however, physical probes perturb the flow field and flame significantly and are thus not adequate for validation measurements.

The cited studies for various atmospheric, and partly turbulent flames, as well as an automotive application, indicate that PAH LIF can provide valuable information on soot formation, specifically when correlated to other optical diagnostics. In the current paper we therefore provide an extension of the existing data in swirl-stabilized pressurized sooting flames by describing the time averaged and representative features of instantaneous PAH distributions as well as their correlation with soot filaments.

2. Experimental setup and PAH spectroscopy

The burner and optical setup have been described in detail in previous publications [36,37]. Minor modifications of the setup were necessary for the actual measurements.

2.1 Burner configuration

The burner consists of three concentric nozzles. Air at room temperature is supplied to the flame through a central (diameter 12.3 mm) and an annular nozzle (inner diameter 14.4 mm, outer diameter 19.8 mm). The air flows are fed from separately controlled plenums and pass radial swirlers consisting of 8 channels for the central nozzle and 12 channels for the annular nozzle. Ethylene is injected in between both air flows through 60 straight channels ($0.5 \times 0.4 \text{ mm}^2$) forming a concentric ring. Air and fuel flows were controlled using electronic mass flow controllers (Bronkhorst) which were carefully calibrated in-house; the accuracy of the calibration is estimated to be below 1% of the maximum flow rates. The exit planes of the fuel and air nozzles are located at the level of the combustion chamber inlet, defined as height $h=0$, allowing for full optical access to the fuel injection. The combustion chamber measures 120 mm in height and has a square section of $68 \times 68 \text{ mm}^2$ with beveled edges (see Fig. 1). Four 3-mm-thick quartz windows ($127 \times 59 \text{ mm}^2$) are mounted between four water-cooled metal posts yielding excellent optical access of $51.4 \times 120 \text{ mm}^2$ to the flame. The water-cooled top plate has a cylindrical exhaust hole (diameter 40 mm, length 24 mm), linked to the combustion chamber by a curvature. The high velocity in the exhaust tube prevents any backflow from outside the combustion chamber. Each of the corner posts has an additional air duct of 5 mm diameter for the injection of secondary air into the combustor at a height of 80 mm. The four radially-injected jets meet on the combustor axis and form a stagnation point. A metal plate shields the burner front plate from the hot combustion gases during operation. This is required because of the lack of external cooling of this part.

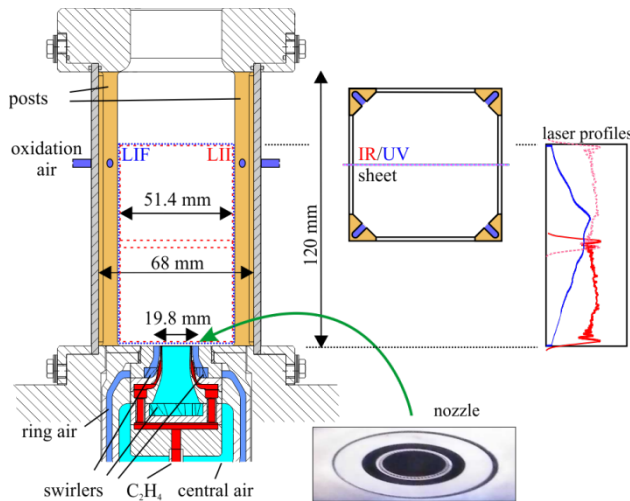


Fig. 1: Burner geometry, nozzle details and cross section at the height of oxidation air injection, with the laser sheet positions and profiles inserted at top right; blue indicates the UV sheet profile, red represents the IR sheet profile in both positions.

The combustor is mounted in a water-cooled steel pressure housing with large optical access ($60 \times 120 \text{ mm}^2$) from 4 sides. The pressure can be adjusted by partially blocking the exhaust port with a movable piston. An air flow through the gap between the combustion chamber and the pressure housing serves as air cooling for the windows of the combustion chamber. The inner surface of the combustor windows does not show significant degradation during operation, but exhibits some soot

deposition at certain operating conditions. The surface temperature is therefore estimated to be between 500 and 900 °C, depending on the position relative to the location of the flame.

2.2 Operating conditions

The combustor was designed for operation at approximately 10 kW/bar thermal power providing Re numbers clearly above 10000 [36]. For the current study a subset of operating points was selected from those presented in [36], including a reference point operating at 3 bar, rich primary combustion with additional oxidation air injection after two thirds of the combustor. This case is compared with the corresponding one without oxidation air; both were also focus of [37]. In addition, an operating point with lean condition ($\phi=0.9$) in the primary zone was chosen in comparison to the reference point to visualize processes close to the rich-lean transition of the flame, where PAH and soot formation are minor. For equivalence ratios slightly below 0.9 in the primary zone the flame makes a sudden transition to a non-sooting (blue) state and exhibits thermoacoustic pulsations. The selected operating conditions are listed in Table 1. The equivalence ratio ϕ and thermal power P were calculated from the primary air flow rate Q_{air} as a sum of central ($Q_{air,c}$) and ring air ($Q_{air,r}$), whereas the global equivalence ratio ϕ_{global} and the global thermal power P_{global} were calculated from the total air flow rate, $Q_{air}+Q_{oxi}$. The amount of oxidation air is given as fraction Q_{oxi}/Q_{air} . Note that due to the excess fuel the value for P is limited by the combustion air mass flow in most cases whereas ϕ_{global} becomes lean after injection of oxidation air and thus P_{global} depends on the fuel mass flow. The air split ratio is defined as the ratio of central air to the total combustion air $Q_{air,c}/Q_{air}$.

The flow field is known to consist of a conically shaped inflow region with relatively high flow velocities, an inner and an outer recirculation zone and the shear layers between the inflow and the recirculating flows [49] which is in agreement with results from similar combustors [50,51].

Table 1. Flame parameters for studied flames: Pressure, p , flow rates for air through burner (central and ring), $Q_{air,c}$ and $Q_{air,r}$, fuel, Q_{fuel} , oxidation air through secondary air inlet, Q_{oxi} , equivalence ratios, ϕ , ϕ_{global} , thermal powers, P , P_{global} , and fractions $Q_{air,c}/Q_{air}$ and Q_{oxi}/Q_{air} with $Q_{air}=Q_{air,c}+Q_{air,r}$. Flow rates in standard liters per minute (slm) are referenced to 1.013 bar and 273 K.

p [bar]	ϕ	$P_{primary}$ [kW]	$Q_{air,c}$ [slm]	$Q_{air,r}$ [slm]	Q_{fuel} [slm]	Q_{oxi} [slm]	$\frac{Q_{air,c}}{Q_{air}}$	$\frac{Q_{oxi}}{Q_{air}}$	ϕ_{global}	P_{global} [kW]
3	0.9	32.2	156.0	365.1	32.7	208.2	0.3	0.4	0.64	32.2
3	1.2	32.2	140.8	328.5	39.3	0	0.3	0	1.2	32.2
3	1.2	32.2	140.8	328.5	39.3	187.4	0.3	0.4	0.86	38.6

2.3 Optical setup

The optical setup described in Ref. [37] has only marginally been modified to allow for simultaneous PAH laser-induced fluorescence (LIF) and laser-induced incandescence (LII) measurements and is shown in Fig. 2. Two different lasers are used for excitation. For LII, the fundamental of a Nd:YAG laser (pulse duration of 7 ns, Brilliant B, Quantel) at $\lambda=1064$ nm is formed into a homogeneous light sheet by a cylindrical ($f=-50$ mm) and a spherical lens ($f=1000$ mm). An approximately 47 mm tall laser sheet of 0.3 mm thickness is created in the measurement plane using a rectangular aperture. The clipped region exhibits a relatively uniform fluence of $0.4 \text{ mJ/cm}^2 \pm 15\%$. The corresponding pulse energy of 55 mJ is set by attenuating the laser beam with a half wave plate and polarizer

combination. A laser sheet similar to the one employed in this study is shown in Fig. 1 (top right plot). A translation stage was used to shift the LII excitation optics reproducibly between an upper and lower sheet position.

LII images are recorded perpendicular to the excitation plane with an image-intensified dual frame CCD camera (DicamPro, PCO) equipped with a Nikon f/2.5 camera lens. The first exposure of 60 ns duration serves to acquire the flame luminosity background immediately before the laser pulse while the second frame captures the first 60 ns of the LII signal.

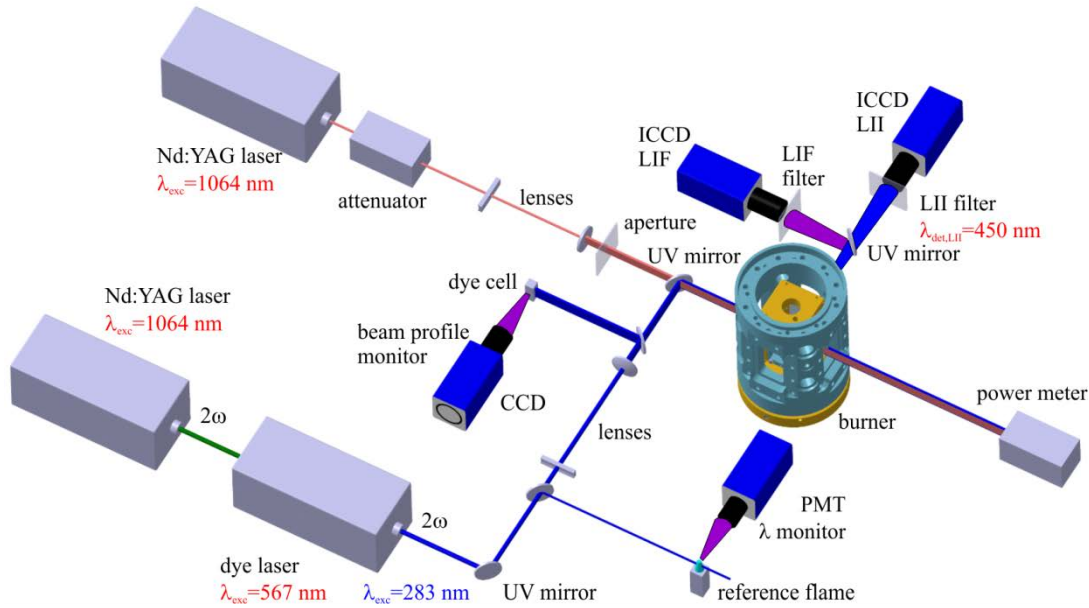


Fig. 2: Optical setup used for simultaneous PAH-LIF and LII experiments.

For excitation of PAH fluorescence, a dye laser (Sirah PRSC-G-24-EG) was pumped by the second harmonic of a Nd:YAG laser (Spectra Physics PIV-400-10). After frequency doubling, pulse energies of approximately 20-30 mJ at 283 nm were used for PAH excitation. The beam was expanded into a sheet of 80 mm height and 0.4 mm waist thickness in the measurement location by using a cylindrical ($f = -50 \text{ mm}$) and a spherical lens ($f = 750 \text{ mm}$). The resulting sheet profile, starting approx. 3 mm above the burner plate, is shown in Fig. 1 (top right plot) together with the LII excitation sheet. PAH molecules were excited by shifting the laser wavelength a bit off the $Q_1(8)$ line of the $A^2\Sigma-X^2\Pi(1,0)$ transition at $\lambda = 283.55 \text{ nm}$ used for OH excitation in [37]. The exact wavelength tuning was validated in a reference burner using a photomultiplier tube equipped with a long pass filter (Schott WG 295) and a band pass filter around 315 nm (Hugo Anders). Shortly before entering the combustor this sheet was combined with the IR sheet by a UV mirror transmitting 1064 nm radiation.

The fluorescence signal emitted at 90° is separated from LII at visible wavelengths by a UV mirror with peak reflectivity between 290 and 340 nm, collected by an achromatic UV lens (Cerro, Sodern 100 mm) and detected by an intensified CCD camera (Imager Pro Plus, LaVision). For PAH PLIF measurements a gate duration of 50 ns and a 300-400 nm band pass filter were employed (UG1, Schott) to reduce background signal. PAH LIF images were corrected for the CCD chip sensitivity. The timing of the fluorescence experiment relative to LII was such that the UV beam crossed the flame 400 ns before the IR beam to prevent interference between the two measurement systems while still having a short enough delay that the measurements are effectively simultaneous. Soot and PAH

images were matched to each other based on a common target image. The determination of the quantitative time-averaged soot distributions has been described recently [36]. In the current study we did not perform a calibration again, but rather used the recently derived calibration constants for image correlation with simultaneously derived PAH distributions.

2.4 PAH spectroscopy and data evaluation

Isolated PAH molecules at low temperature exhibit spectrally well-isolated absorption and emission features in the UV and visible spectral range [52] allowing for the discrimination of single components [53]. At flame conditions, however, PAH spectroscopy becomes complex (see for example [41]): different yet similar PAH species with significantly different optical properties (molecular energy levels, absorption cross sections, Boltzmann factors), are present in rich flames. They span a wide concentration range, the absorption and emission features broaden due to line-overlap, and collisional quenching of fluorescence based on local gas composition and temperature vary. Therefore, only sampling techniques allow for a detailed (ex-situ) analysis with focus on single species [41,47,48]. Based on the above mentioned challenges, in-situ PAH-LIF measurements have to be considered with caution with respect to relative intensities. Nevertheless, PAH monitoring still can provide valuable information, specifically when correlated with distributions of other species. Leermakers and Bejaoui [46,54] selected the excitation wavelength (and detection range) to focus on specific size-classes of PAH. This is based on the fact that the absorption and emission spectra of PAH molecules shift to longer wavelengths with increasing number of rings [54,55]. Our excitation wavelength of about 283 nm mostly excludes one-ring PAH (benzene, toluene) while the chosen detection range with sensitivity between 300 and 350 nm restricted the selection to small, i.e. two to four-ring PAH.

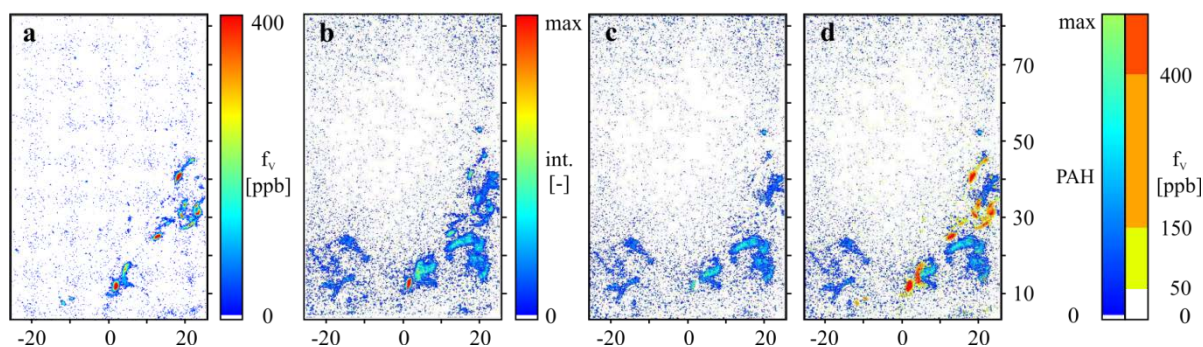


Fig. 3: Analysis of PAH LIF images (b) excited in the UV by subtraction of the simultaneously IR excited soot (a) to yield an image consisting of pure PAH (c), and addition of the color-coded soot distribution (d). The image size corresponds to the area excited by the UV light sheet, while the IR sheet was applied in the bottom position. The pair of color bars corresponds to (d), the single color bar on the left applies to (a)-(c).

Compared to the OH LIF experiment presented in [37], some experimental modifications were employed to optimize PAH LIF signals as described in the section on the experimental setup. Besides tuning the excitation wavelength slightly away from the OH absorption line and replacing the narrowband OH detection filter by a color glass filter transmitting light between 300 and 400 nm, we had to increase the pulse energy by approximately a factor of five and increase the image intensifier settings to generate sufficient fluorescence signal. With the increased pulse energy, the laser sheet used for PAH LIF excitation was sufficiently strong to co-excite some LII in the low to intermediate

fluence range of the typical LII response curve. Close to the low-energy wings of the laser sheet, i.e. the upstream and downstream edge of the LIF images, no LII excitation was identified indicating that fluences were below the onset of LII excitation (see UV sheet profile in Fig. 1). The simultaneously employed IR laser served to identify soot events co-excited by the UV laser. However, because the fluence in the UV laser sheet is not continuously in the LII plateau regime, the UV-excited LII signal does not linearly correlate to soot concentration. Therefore, subtraction of the IR-excited images from the raw PAH images might suffer from overcorrection, and as a result, existence of soot in a certain location does not allow distinguishing whether PAH are co-existing or not. However, as the image area covered by soot is typically relatively small, this does not significantly impact the argumentation of the following sections. The procedure of data analysis is presented in Fig. 3. Fig. 3a shows the IR-excited soot distribution, Fig. 3b represents the common soot and PAH emission induced by the UV laser pulse. Fig. 3c is corrected for soot by subtracting the pure soot distribution with an arbitrary but fixed factor (which was deduced from one sequence and subsequently applied to all others) and presents the undisturbed PAH distribution. The final Fig. 3d combines the distributions from Figs. 3a and c to visualize how soot and its precursor species PAH correlate.

For calculation of ensemble averaged PAH LIF images, a segmentation filtering routine has been employed. This serves to reduce the impact of image intensifier noise in regions of low laser sheet intensity by removing round structures below six pixels in diameter.

3. Results

The following section starts with a detailed characterization of the reference flame, which is a rich flame at 3 bar with additional oxidation air injection (third flame in Table 1). This includes the correlation of instantaneous PAH and soot distributions and that of time-averaged OH, PAH and soot distributions. The main differences between the flames with and without this secondary air are then presented. The comparison demonstrates the impact of this air which is convected far upstream towards the injector by the inner recirculation zone. Finally, a flame with very low soot production is characterized (first flame in Table 1). It presents a validation case which might be appropriate for numerical simulations with simplified soot models.

3.1 Rich combustion with oxidation air

Exemplary results from correlated measurements at the reference operating point with additional oxidation air are displayed in Figs. 3 and 4a. Fig. 4a shows the bottom portion of Fig. 3d. The blue colored regions labelled “1” are isolated PAH clouds, regions labelled “2” only show up in the IR-excited image and represent isolated (transported) soot while those labelled “3” show the transition from PAH into soot. The blue PAH cloud at top right contains two tiny red dots indicating soot inception inside a PAH volume. Fig. 4c shows two distinct soot structures of similar shape upon IR excitation, i.e. soot. The composite plot Fig. 4b shows a completely different history of both soot events. While the one appears to be isolated, transported soot (2), the other one (3) forms the edge of a large PAH cloud thus monitoring the transition from PAH into soot; obviously, the soot filaments have a different formation history which depends on the temperature and composition history of the respective fluid elements. Those examples show that unlike soot, PAH signatures are typically larger, exhibit a more homogeneous intensity and lower intensity dynamics.

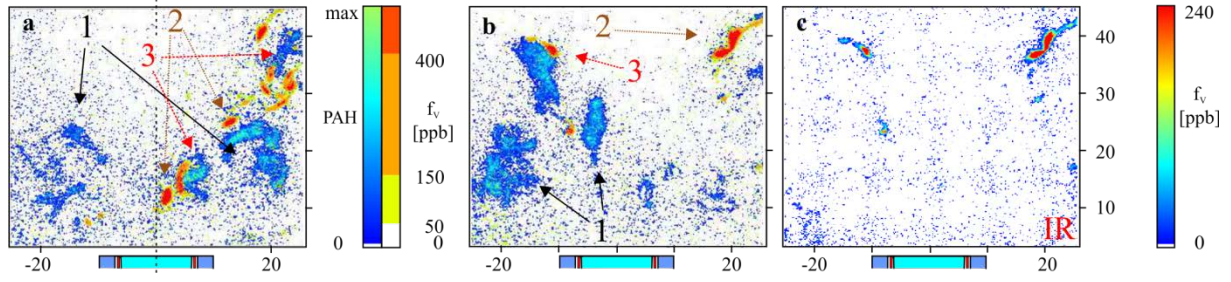


Fig. 4: (a) shows some features of PAH-soot correlation from Fig. 3d in more detail (reference case). The merged PAH/soot distribution recorded at another instant shown in (b) clearly shows a different formation history of both prominent soot features present in the IR-only excited image (c). The combined color bars correspond to the overlaid plots (a) and (b).

In jet flames, soot-related processes (soot formation, mixing and oxidation) occur in spatially separated regions [32,56] and these are typically stretched out along the mean flow direction. In swirl-stabilized combustors, the flow field is more complex and mixing is faster than in jet flames. Therefore, conditions favorable for soot formation or oxidation can prevail at various locations. The measurements showed that soot structures in the swirl flames under investigation are smaller than those in jet flames. Also, due to the complex flow field it is difficult to distinguish between mature soot and nascent soot without further information. Here, the simultaneously measured PAH LIF distributions help to interpret the soot history correctly. For illustration, some exemplary plots are shown in Fig. 5, ordered by increasing soot load. The sequence clearly visualizes the high intermittency of soot for this operating condition which, due to the faster mixing, is even higher than results from jet flames [32,33,56]. Large intensity variations are seen within the series, the location and size of soot-containing areas within an image changes significantly and the dynamics within single soot filaments is large. In contrast, the PAH distributions exhibit a more uniform intensity, the structures are always present at similar total covered area per image, and have mostly larger size than soot structures. All these properties seem relatively independent from the soot characteristics of the respective image. Therefore the following section focusses on spatial correlations in more detail.

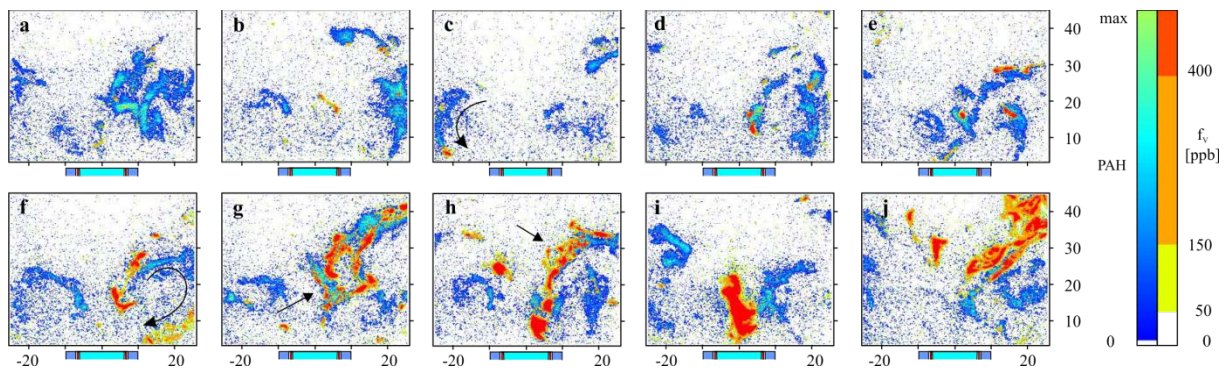


Fig. 5: Some exemplary plots showing different types of PAH/soot correlation (reference case). Images are ordered for increasing soot load.

The examples displayed in Fig. 5 show the different states of soot formation progress in relation to PAH distributions. In the first frames, small soot islands of less than 1 mm diameter are attached to larger PAH structures up to 20 mm long and few mm wide. Some of the soot islands are found within

the PAH clouds but frequently they are located at the periphery of the PAH structures. It seems reasonable to interpret such events as soot in an early stage of formation, i.e. where soot is formed from the surrounding PAH clouds. The soot structures are found on different sides of the PAH clouds and there is no preferred direction of soot formation from PAH identifiable. The examples displayed in Fig. 5f-g demonstrate how larger soot structures of 5 to 10 mm length and approximately 2 mm thickness are related to PAH distributions. Fig. 5 g and h give the impression that the transition from PAH to soot has reached an advanced stage. Finally, most of the PAH bath seems to be converted to soot, as shown by the large soot structures (up to $20 \times 5 \text{ mm}^2$) in Fig. 5 i and j. It should be kept in mind that soot can persist for some time in the flame. During its residence time it is convected by the flow field and thus it can happen that mature soot structures are detected that are not correlated to PAH fields. In contrast to the characterization of turbulent jet flames by Lee et al. [32], size, shape and intensity of the LII images show much larger variations (note the described incipient soot islands in Fig. 5 a and b), with trends not clearly linked to a specific location in the flame. Here, continuous soot islands become visible at sizes as small as 1 mm, and never reach lengths significantly more than 20 mm.

In addition to the different stages of soot growth, Fig. 5 yields an impression of the influence of the turbulent flow field on the observed structures. The wrinkles in the distributions are most likely related to turbulent flow structures. Also, in some instances the shapes of the PAH and soot structures resemble the vortices of the flow field, as indicated in Fig. 5 d and f.

More insight into soot formation chemistry might be accessible in the stages of soot formation displayed in Fig. 5g and h. The labelled regions contain a field of increasingly strong soot inception islands of varying intensities embedded in a larger PAH area, which typically show quite homogeneous intensities throughout the sequence. The considerably different soot loads in regions of similar homogenous PAH fluorescence, e.g. in Fig. 5 a and g might be explained by the influence of other species relevant to soot formation but not monitored in our experiment, as for example acetylene [57].

The above discussion of the selected images of soot/PAH correlation shows the diversity of the soot formation process in turbulent swirl flames. It will be interesting to see whether LES simulations will yield similar structures.

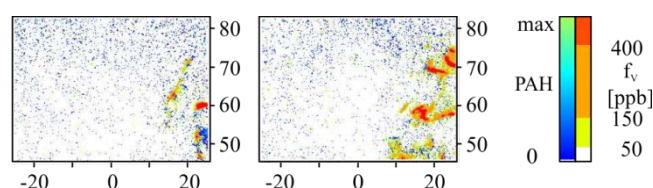


Fig. 6: In the downstream field of view only low PAH intensity, mainly associated with soot, is left over from consumption either by growth into soot or by oxidation.

Only few PAH clouds persist into the downstream LII laser sheet position. Lee et al. attributed the disappearance of PAH fluorescence in turbulent jet flames as a result of intense mixing. Examples for this region reaching from $h=45$ to 82 mm are shown in Fig. 6; no PAH are identified close to the downstream end of the images of this sequence. The imaged region is dominated by transported soot. No isolated PAH clouds are identified. If a signal can be attributed to PAH here, it is closely

attached to a soot filament and relatively small in size, as shown in Fig. 6. It is thus concluded, that PAH are either consumed by soot formation and growth or oxidized in this part of the combustor.

Fig. 7 a-c shows the PAH distribution averaged over 200 instantaneous images together with those of OH and soot (distributions from [36,37]) for the reference flame with oxidation air. The dark horizontal lines in the image are probably due to persistent soot deposits on the laser entrance window of the combustor. For convenience, the soot distribution is added to the OH and PAH plots as red contour. It is important to note that the apparent overlap of the OH and soot distributions is due to ensemble-averaging of multiple instantaneous images; simultaneously recorded instantaneous distributions of OH and soot never overlapped [37,56]. As for the OH LIF measurements, the PAH LIF images show a right-left asymmetry due to laser absorption on the passage through the flame from right to left. Thus information from the right side of the combustor is more reliable, and has been used for the representation of intermittency maps in the right portion of the figure (d-f). These represent the fraction of presence of a species in a certain location within the whole sequence; high intermittency is characterized by a low fraction or intermittency index, as defined for example in [32,33]. The OH distribution (Fig. 7a) is characterized by a distinct in-flow region of cold fresh gas without any signal close to the nozzle. It is enclosed by high OH concentrations formed in the flame zone which is located in the shear layer between the fresh gas in-flow and recirculated hot combustion products, and high concentrations in the inner recirculation zone. For instantaneous OH distributions in this flame we refer to [37].

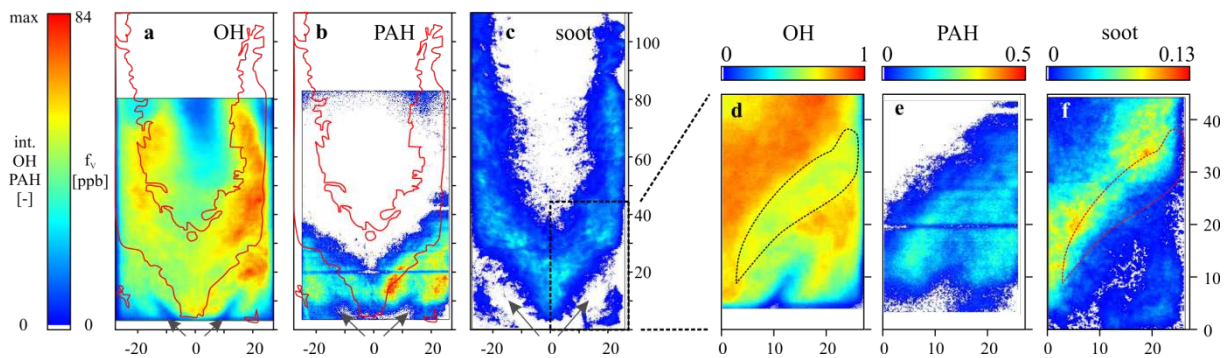


Fig. 7: Ensemble-averaged distributions of OH, soot [36,37] and PAH (a-c) for the reference operating point at 3 bar, rich primary combustion with secondary oxidation air injection. The continuous contours in the OH and PAH plots show the soot distribution. The right portion of the figure (d-f) shows the fraction of images of the sequence with the respective species present for the soot formation region.

For PAH, the in-flow region can be recognized by negligible signal levels. As for OH this low-signal region is enclosed by PAH signal. The PAH plot receives its smoothness due to the homogeneous intensities of instantaneous PAH clouds and their wide spatial fluctuations. In contrast to OH, PAH intensities are minimal close to the burner axis, and a conical region central to the inner recirculation zone remains almost PAH-free. A similar signal-free region exists for the respective soot distribution (c) shifted slightly downstream, thus soot persists further into the inner recirculation zone than PAH. This region, partly fed by the secondary oxidation air, is characterized by relatively high OH levels, so both PAH and soot eventually become oxidized and disappear. Unlike PAH, the soot distribution is characterized by residual structure originating from tiny instantaneous soot filaments of high dynamics in combination with the high intermittency of soot. The intermittency index of soot (Fig.

7f), indicating the fraction of images containing soot in a certain location, remains close to 0.1 independent of vertical distance from the injector (see [36], exact values depend on the threshold level used to distinguish between intensifier noise and soot). This very low value, compared to results in turbulent jet flames [32], does not show any clear trend along the branches of the v-shaped soot distribution. It indicates the relatively good mixture generated by the highly turbulent swirling flow, and explains why ensemble-averaged soot concentrations are significantly lower than those described for jet flames [32,35].

PAH occur slightly downstream compared to OH. Further downstream PAH and soot distributions show some overlap. A few millimeters downstream and towards the inner recirculation zone the transition from PAH into soot appears, and also upstream into the outer recirculation zone. In contrast to soot, the intermittency index for OH, i.e. the fraction of images with OH present (Fig. 7d), is very high throughout the figure, typically beyond 0.5. A slight dip by roughly 10% is labeled in the respective intermittency plot in Fig. 7d by a dashed contour. This region separates the primary combustion zone fed by the combustion air / fuel mixture and the secondary combustion zone where the additional oxidation air interacts with unburnt hydrocarbons which leave the rich primary combustion zone [37]. The complementary behavior of soot and OH in this region is shown in [37], preventing instantaneous co-existence of both species. Consequently, the dip presented in the OH intermittency map correlates well with presence of soot in a respective number of images, i.e. increased values in the soot intermittency plot. Major soot formation is closely correlated to this dip in the OH intermittency plot situated between primary and secondary combustion zones, and coincident with highest values of the soot intermittency index and soot concentrations (Fig. 7c and f). Regions of significant soot concentrations yet low PAH intensities show the persistence of transported, mature soot which is isolated from PAH (close to combustor axis and along soot wings reaching far downstream). It is important to note that comparison of PAH and soot distributions allows the identification of soot close to the burner axis, upstream in the inner recirculation zone, as transported or isolated from PAH. Here, at heights between 12 and 24 mm, CARS experiments [37] determined average temperatures clearly above 2000 K. Instantaneous temperatures never drop below 1750 K, which is unfavorable for soot formation [58,59]. Therefore, soot must have been formed elsewhere and transported into this region where the ensemble-averaged soot concentration peaks. Instantaneous representations of this (soot transport towards the injector) are Figs. 5h and i. In general, soot is mainly distributed along the upstream edge of the conical inner recirculation zone where transport and convection times are sufficiently long and locally rich conditions between the primary combustion zone and the secondary-air induced combustion can persist. Here, average temperatures are also determined to be above 2000 K, but contrarily to the on-axis positions, about 10% of the instantaneous temperatures show values between 1500 and 1750 K. This region is mainly coincident with the downstream portion of the PAH distribution. Further downstream PAH fluorescence is absent, and soot gets oxidized when coming in contact with OH generated by the secondary combustion zone. Lee et al. [32] analyzed independently measured maximum values of ensemble-averaged OH and soot signals, and attributed the overlap of soot and OH fields to the soot-oxidation region of turbulent diffusion flames. Looking at the correlation of instantaneously acquired image pairs, however, indicates that OH and soot typically do not overlap, even in this region [37], confirming the results from time-resolved OH-soot correlations in a jet flame [56]. The impact of oxidation becomes more evident in the following section which compares to the corresponding flame with the oxidation process being switched off.

3.2 Rich combustion without oxidation air

Fig. 8 shows some representations of the case without additional oxidation air, again roughly ordered by soot content. As known from previous studies [36] omission of secondary air changes the instantaneous soot distribution significantly. The inner recirculation zone is mostly covered with scattered soot filaments of varying size and intensity. As for the case with oxidation air, instantaneous PAH distributions show a quite homogeneous appearance throughout the sequence with respect to size and intensity. PAH are mainly present in a V-shaped region, enclosing a more or less intense soot-containing area. Even in the strongly sooting cases shown in the last three frames, isolated PAH clouds exist that have not yet reached conditions to transform into soot. As for the reference case, soot appears upstream the first PAH event.

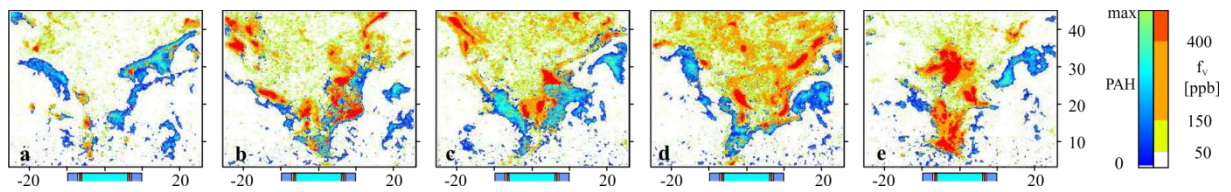


Fig. 8: Some exemplary plots showing different types of PAH/soot correlation (no secondary oxidation air injection). Images are ordered for increasing soot load.

The first frame of the sequence is characterized by tiny soot filaments of approximately 1 mm in size which occur either isolated or as inception islands embedded in a PAH structure. Concentration and size of these embedded soot islands increase significantly in the next frame, while the following examples mainly show relatively intense soot structures with dimensions of about 5 mm attached to the downstream side of the PAH clouds. In addition, soot is present in tiny scattered elements in the central inner recirculation zone. These show an increased number density and intensity and cover the inner recirculation zone almost continuously in Fig. 8d. As mentioned in the data analysis section, existence of soot prevents unambiguous identification of underlying PAH. However, in the images with low soot concentration in the central inner recirculation zone, like Fig. 8a and b, PAH signal can hardly be seen. This suggests that PAH concentrations are generally very low in that region. Finally, most soot concentrates in big chunks of 10 to 15 mm size without the additional spread of tiny soot elements in Fig. 8e. Links to PAH structures are minor, so we interpret these relatively large soot elements as transported mature soot. Their compact structure indicates that these structures have not been subject to significant wrinkling by the turbulent flow field. Unlike in the reference flame, the intermittency index of soot for this region of the flame reaches values of 0.18 [36], still significantly lower compared to typical values in the turbulent jet flames characterized by Lee et al. [32].

In contrast to the reference flame, soot can persist into the central part of the visible flame when the process of oxidation is switched off by omitting quench air. This region is characterized by instantaneous temperatures never dropping below 1750 K. For this flame condition only the processes of soot formation and mixing as categorized by Lee et al. maintain. Regions central in the flame show a slightly different soot pattern relative to regions of primary soot formation at the upstream edge of the soot distribution. This is visualized in Fig. 9 showing the probability density function of soot concentrations for two locations (3x3 pixel in size) within the soot formation zone and one inside the inner recirculation zone. All of them are characterized by a peak at low nominal soot concentration attributed to image intensifier noise. While both positions close to the edge of

the soot distribution exhibit few occurrences of significant soot concentrations, no soot concentrations higher than 0.2 ppm are identified central in the flame. While soot formation in the rich primary combustion zone is expected to occur similar to the respective flame with oxidation air, the region reaching from the central inner recirculation zone downstream is now mostly dominated by transport and mixing. This results in a fragmentation of most soot clouds due to turbulence.

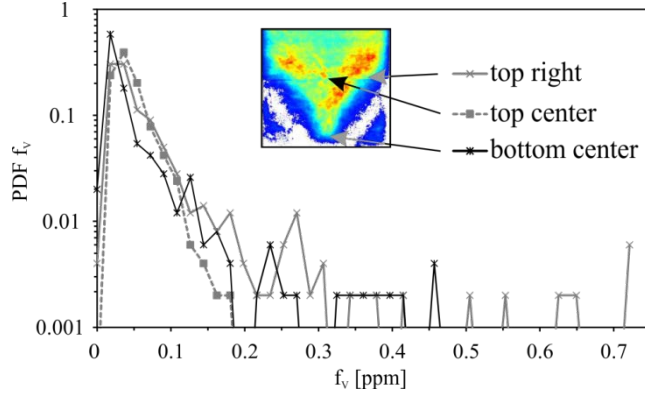


Fig. 9: Probability density functions of soot concentrations found along the soot formation region compared to the central inner recirculation zone in absence of oxidation. For the top center position no soot concentrations above 0.2 ppm are identified.

Due to abundantly existing soot in the downstream LII sheet position, and the fact that no significant PAH activity was detected, this region is not discussed in detail.

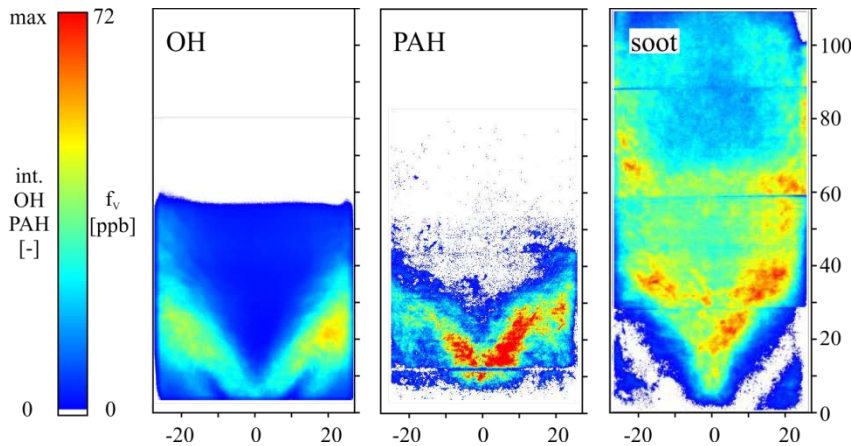


Fig. 10: Comparison of ensemble-averaged PAH distribution to those of OH, soot [36,37] for combustion at 3 bar, rich primary combustion without secondary oxidation air injection.

The specific features presented above result in an ensemble-averaged PAH distribution shown in Fig. 10. The shape of the distribution is similar to the case with oxidation air: two V-shaped branches of main PAH presence slightly downstream of OH, and low intensity in the central inner recirculation zone (note that the PAH signal in this region might be covered by soot due to overcorrection of the PAH images for soot). Unlike the case with oxidation air, the PAH distribution has close resemblance to the OH distribution which here is limited to the upstream region of the combustor. The ensemble-

averaged PAH distribution partly overlaps with the soot distribution; this is particularly the case for regions enclosing the fresh-gas injection, while on the burner axis soot is present closer to the injector than PAH. Unlike the reference case with oxidation air, PAH are present on the flame axis close to the injector to a significant amount. At temperatures which are approximately 350 K cooler compared to the reference flame in this location PAH can survive and thus can contribute to local soot formation.

Similar to the case with oxidation air, the size of the low-signal in-flow region increases from OH over PAH to soot. For OH and soot, this region is well-defined while the PAH distribution remains much more diffuse in this zone. Because in-flow conditions are similar for the test cases with and without oxidation air injected far downstream, soot formation similarly occurs slightly downstream from first PAH occurrence here.

3.3 Lean combustion with oxidation air

When the equivalence ratio of the primary combustion was reduced to 0.9 the flame still appeared orange, but the soot load became very small. Single shot LII images (no examples shown) rarely display soot filaments. If they appear, they are typically isolated from each other and show a similar spatial correlation to PAH as presented for the reference case, i.e. soot inception and formation as well as isolated soot events. In contrast to both rich cases where PAH intensities were homogeneous and PAH areas relatively uniform, the intensity and total PAH area per image show significantly more dynamics. Here, images of negligible or low PAH signal intensity exist, as well as others similarly strong as those shown for the reference case. Under these conditions, PAH formation appears to start in regions which are locally slightly rich.

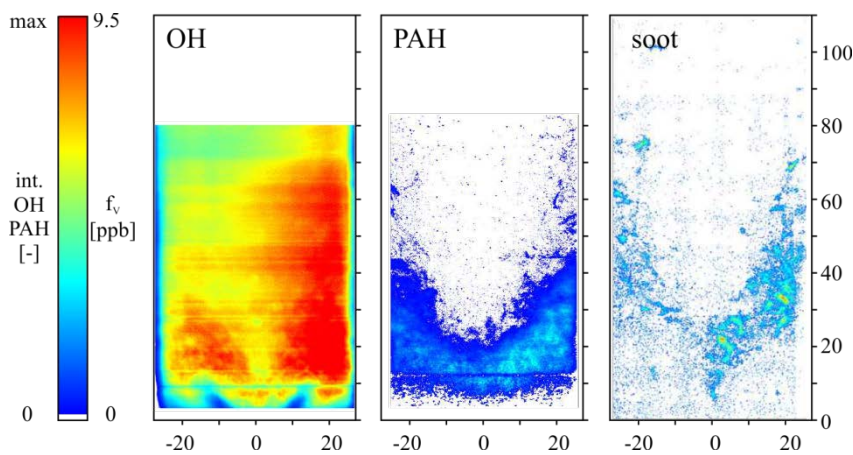


Fig. 11: Comparison of the ensemble-averaged PAH distribution to those of OH and soot for combustion at 3 bar, at moderately lean primary combustion with secondary oxidation air injection.

Consequently, the resulting ensemble-averaged PAH distribution for this case, shown in the middle frame of Fig. 11, exhibits lower intensities than in the reference case (note that the color scale for the averaged PAH distributions is identical for all flames shown). A wide region in the inner recirculation zone is free of PAH, but in the region close to the nozzle the peak intensities are similar to those for the other cases. Low in the inner recirculation zone on the flame axis we identified PAH intensities which are comparable to other regions of the respective distribution. For the rich case with oxidation air described above the PAH intensities were minimal here. This is probably due to the change in

temperature. CARS measurements low in the inner recirculation zone (not shown) indicate a significantly higher proportion of temperatures below 2000 K compared to the reference case, in agreement with the globally lean condition. The decreased temperature in this region is more favorable for soot formation chemistry and allows both PAH and soot to be present. In the downstream portion of the combustor no significant PAH signal is detected. PAH can only exist upstream of the reach of oxidation air which is impacting the central inner recirculation zone. The correlated ensemble-averaged soot distribution is dominated by single events; soot statistics for this weakly sooting operating point is insufficient to provide a smooth image. However, the shape of the soot distribution is similar to that of the reference operating point.

The above discussion on the different operating points focusses on correlations visualized in the plane of excitation. It must be kept in mind that the flow field in this type of swirl combustor is significantly three-dimensional, and with the given optical setup the effect of out-of-plane motion cannot be evaluated. Thus it is not possible to distinguish between apparent isolated, transported soot structures and those which are chemically supplied by PAH fluid elements outside the imaging plane. Nevertheless, we suspect that the described correlations are realistic representations of the processes in this combustor; the instantaneous as well as ensemble-averaged distributions and spatial correlations are well suited for comparison with CFD model results, specifically in combination with detailed information on temperature statistics [37] and velocity field information [49].

4. Conclusions

A swirl stabilized gas turbine model combustor for partially premixed flames was studied with simultaneous PAH-LIF/LII measurements to determine the PAH distribution and identify correlations of soot and small PAH serving as soot precursors. This extends the data basis already published, for use as validation data in numerical simulation. The data presented include three test cases differing in the equivalence ratio of the primary combustion and the addition of secondary oxidation air that can be injected downstream of the main combustion. For all cases, isolated soot and PAH structures were detected as well as PAH growing into soot at varying intensity, from tiny soot inception islands up to the growth into mature soot. By correlation with the respective PAH distribution different soot formation histories could be identified. For rich operation of the primary combustion zone, mostly isolated PAH clouds show a relatively homogeneous intensity without significant intensity fluctuations within a sequence of 200 instantaneous images. This is in contrast to soot that generally showed much stronger dynamics. For leaner operating conditions, less soot-containing images are detected, and PAH characteristics are different from those in both rich flames: the size and intensities of PAH structures show larger variations on a lower average level. The significantly different combinations of PAH and soot structures highlight the extremely wide range of different local conditions contributing to the formation of mature soot, and later consumption. One prominent feature in the instantaneous distributions is the formation of vortical structures either by PAH alone or in combination with soot filaments. In contrast to soot, the PAH signal intensity in the reference flame is minimal close to the burner axis in the upstream inner recirculation zone. This is in correlation with high temperatures close to the stagnation point, being unfavorable for soot formation. Consequently, soot presence there is due to transport, not to chemical reaction. Further downstream the PAH signal intensity decreases indicating the consumption either by transformation into soot or by oxidation which is initiated by the secondary air added after two thirds of the combustor. For the primary combustion zone, the ensemble-averaged PAH distribution shows more similarities with OH than with the soot distribution. PAH formation starts slightly delayed relative to

OH while PAH occur in regions attributed to the fresh-gas inflow which are still soot-free. We encourage modelers to use the experimental data for the validation of their codes.

Acknowledgements

Part of this work was funded by the European Commission within the Project Fuel Injector Research for Sustainable Transport (FIRST) under Contract No. 265848.

Compliance with Ethical Standards

This manuscript complies with the ethical rules of Applied Physics B.

References

- [1] T.R. Barfknecht: Prog. Energ. Combust. 9, 199 (1983).
- [2] C. Dasenbrock, L. Peters, O. Creutzenberg, U. Heinrich, Toxicol. Lett. 88, 15 (1996).
- [3] D.S. Lee, D.W. Fahey, P.M. Forster, P.J. Newton, R.C.N. Wit, L.L. Lim, B. Owen, R. Sausen: Atmos. Environ. 43, 3520 (2009).
- [4] C. Eberle, T. Blacha, P. Gerlinger, M. Aigner, Numerical Simulations of Soot and NO_x Distributions in a Full Scale Aero-Engine Combustor at Two Different Flight Altitudes, Proc. 52nd AIAA Aerospace Sciences Meeting 2014, Paper AIAA 2014-0132, doi 10.2514/6.2014-0132.
- [5] M. Mueller, H. Pitsch: Physics of Fluids 25, 110812 (2012).
- [6] T. Blacha, M. Di Domenico, M. Rachner, P. Gerlinger, M. Aigner: Modeling of soot and NO_x in a full scale turbine engine combustor with detailed chemistry, Proc. ASME Turbo Expo 2011, GT2011-45084.
- [7] F. Xu, P.B. Sunderland, G.M. Faeth: Combust. Flame 108, 471 (1997).
- [8] B. Axelsson, R. Collin, P.-E. Bengtsson: Appl. Opt. 39, 3683 (2000).
- [9] A.V. Menon, S.-Y. Lee, M.J. Linevsky, T.A. Litzinger, R.J. Santoro: Proc. Comb. Inst. 31, 593 (2007).
- [10] C. Brackmann, J. Bood, P.-E. Bengtsson, T. Seeger, M. Schenk, A. Leipertz: Appl. Opt. 41, 564 (2002).
- [11] R. Hadeef, K.P. Geigle, W. Meier, M. Aigner: Int. J. Thermal Sci. 49, 1457 (2010).
- [12] H. Bladh, J. Johnsson, N.-E. Olofsson, A. Bohlin, P.-E. Bengtsson: Proc. Comb. Inst. 33, 641 (2011).
- [13] S. De Iuliis, S. Maffi, F. Migliorini, F. Cignoli, G. Zizak: Appl. Phys. B 106, 707 (2012).
- [14] D.R. Snelling, K.A. Thomson, G.J. Smallwood, Ö.L. Gülder: Appl. Opt. 38, 2478 (1999).

- [15] D.R. Snelling, F. Liu, G.J. Smallwood, Ö.L. Gülder: Combust. Flame 136, 180 (2004).
- [16] B.M. Crosland, M.R. Johnson, K.A. Thomson: Appl. Phys. B 102, 173 (2011).
- [17] F. Migliorini, K. A. Thomson, G. J. Smallwood: Appl. Phys. B 104, 273 (2011).
- [18] D.R. Snelling, O. Link, K. A. Thomson, G. J. Smallwood: Appl. Phys. B 104, 385 (2011).
- [19] R.J. Santoro, H.G. Semerjian, R.A. Dobbins: Combust. Flame 51, 203 (1983).
- [20] R.J. Santoro, T.T. Yeh, J.J. Horvath, H.G. Semerjian: Combust. Sci. Technol. 53, 89 (1987).
- [21] C.M. Megaridis, R.A. Dobbins: Proc. Combust. Inst. 22, 353 (1988).
- [22] C.M. Megaridis, R.A. Dobbins: Combust. Sci. Technol. 66, 1 (1989).
- [23] R. Puri, T.F. Richardson, R.J. Santoro, R.A. Dobbins: Combust. Flame 92, 320 (1993).
- [24] I.M. Kennedy, C. Yam, D.C. Rapp, R.J. Santoro: Combust. Flame 107, 368 (1996).
- [25] C.S. McEnally, U.O. Köylü, L.D. Pfefferle, D.E. Rosner: Combust. Flame 109, 701 (1997).
- [26] U.O. Köylü, C.S. McEnally, D.E. Rosner, L.D. Pfefferle: Combust. Flame 110, 494 (1997).
- [27] A.G. Yazicioglu, C.M. Megaridis, A. Campbell, K.O. Lee, M.Y. Choi: Combust. Sci. Technol. 171, 71 (2001).
- [28] S.S. Iyer, T.A. Litzinger, S.Y. Lee, R.J. Santoro: Combust. Flame 149, 206 (2007).
- [29] C.P. Arana, M. Pontoni, S. Sen, I.K. Puri: Combust. Flame 138, 362 (2004).
- [30] International Sooting Flame Workshop Series,
<http://www.adelaide.edu.au/cet/isfworkshop/current/>, accessed on Nov. 11, 2014.
- [31] A. Coppalle, D. Joyeux: Combust. Flame 96, 275 (1994).
- [32] S. Lee, S.R. Turns, R.J. Santoro: Combust. Flame 156, 2264 (2009).
- [33] N.H. Qamar, Z.T. Alwahabi, Q.N. Chan, G.J. Nathan, D. Roekaerts, K.D. King: Combust. Flame 156, 1339 (2009).
- [34] J. Zhang, C.R. Shaddix, R.W. Schefer: Rev. Sci. Instrum. 82, 074101 (2011).
- [35] M. Köhler, K.P. Geigle, T. Blacha, P. Gerlinger, W. Meier: Combust. Flame 159, 2620 (2012).
- [36] K.P. Geigle, R. Hadeif, W. Meier: J. Eng. Gas Turbines Power 136, 021505 (2014).
- [37] K.P. Geigle, M. Köhler, W. O’Loughlin, W. Meier: Proc. Comb. Inst. 35, 3373 (2015).
- [38] S. Drennan, T. Malewicki, Z. Luo, K. Davis, G. Goldin: Simulations of soot volume fraction and size distribution in a high pressure non-premixed ethylene flame using a detailed mechanism, submitted to ASME IGTI 2015, GT2015-43594.

- [39] B. Franzelli, E. Riber, B. Cuenot, M. Ihme: Numerical Modeling of Soot Production in Aero-engine Combustors using Large Eddy Simulations, submitted to ASME IGTI 2015, GT2015-43630.
- [40] M. Frenklach, H. Wang, Proc. Combust. Inst. 23, 1559 (1990).
- [41] P. Desgroux, X. Mercier, K.A. Thomson: Proc. Comb. Inst. 34, 1713 (2013).
- [42] Vander Wal, Proc. Comb. Inst. 26, 2269 (1996).
- [43] C. Schoemaeker Moreau, E. Therssen, X. Mercier, J. Pauwels, P. Desgroux: Appl. Phys. B 78, 485 (2004).
- [44] K.C. Smyth, C.R. Shaddix, D.A. Everest: Combust. Flame 111, 185 (1997).
- [45] M.A. Mikofski, T.C. Williams, C.R. Shaddix, A.C. Fernandez-Pello, L.G. Blevins: Combust. Flame 149, 463 (2007).
- [46] C.A.J. Leermakers, M.P.B. Musculus: Proc. Comb. Inst. 35, 3079 (2015).
- [47] M. Wartel, J.-F. Pauwels, P. Desgroux, X. Mercier: J. Phys. Chem. A 115, 14153 (2011).
- [48] A. Keller, R. Kovacs, K.H. Homann: Phys. Chem. Chem. Phys. 2, 1667 (2000).
- [49] M. Stöhr, K.P. Geigle, W. Meier: unpublished data, "Correlated velocity and soot measurements in a gas turbine model combustor", in preparation for publication.
- [50] P. Weigand, W. Meier, X.R. Duan, W. Stricker, M. Aigner: Combust. Flame 144, 205 (2006).
- [51] K.P. Geigle, J. Zerbs, M. Köhler, M. Stöhr, W. Meier: J. Eng. Gas Turbines Power 133, 121503 (2011).
- [52] I.A. Nakhimovsky, M. Lamotte, J. Jousot-Dubien: Handbook of low temperature electronic spectra of polycyclic aromatic hydrocarbons, Elsevier, Amsterdam, 1989.
- [53] K.P. Geigle, G. Hohlneicher: J. Mol. Struct. 480-481, 247 (1999).
- [54] S. Bejaoui, X. Mercier, P. Desgroux, E. Therssen: Combust. Flame 161, 2479 (2014).
- [55] K. Hayashida, K. Amagai, K. Satoh, M. Arai: J. Eng. Gas Turbines Power 128, 241 (2006).
- [56] B. Franzelli, P. Scouflaire, S. Candel: Time-resolved spatial patterns and interactions of soot, PAH and OH in a turbulent diffusion flame, Proc. Combust. Inst. 35, 1921 (2015).
- [57] C. Eberle, P. Gerlinger, K.P. Geigle, M. Aigner: Soot Predictions in an Aero-Engine Model Combustor at Elevated Pressure Using URANS and Finite-Rate Chemistry, submitted to Combust. Sci. Technol.
- [58] H. Bockhorn: Soot Formation in Combustion, Springer Verlag, Berlin-Heidelberg-New York, 1994, pp. 149 ff.
- [59] H. Jander, N. Petereit, D.M. Razus: Z. Phys. Chem. 188, 159 (1995).